# *Towards quantifying the reaction network around the sulfate–methane-transition-zone in the Ulleung Basin, East Sea, with a kinetic modeling approach*





| | |
|---|---|
| **Citation** | Hong, W. L., Torres, M. E., Kim, J. H., Choi, J., & Bahk, J. J. (2014). Towards quantifying the reaction network around the sulfate-methane-transition-zone in the Ulleung Basin, East Sea, with a kinetic modeling approach. Geochimica et Cosmochimica Acta, 140, 127-141. doi:10.1016/j.gca.2014.05.032 |
| **DOI** | 10.1016/j.gca.2014.05.032 |
| **Publisher** | Elsevier |
| **Version** | Accepted Manuscript |
| **Terms of Use** | http://cdss.library.oregonstate.edu/sa-termsofuse |

# Towards quantifying the reaction network around the sulfate-methane-transition-zone in the Ulleung Basin, East Sea, with a kinetic modeling approach

Wei-Li Hong[1], Marta E. Torres[1], Ji-Hoon Kim[2], Jiyoung Choi[2], Jang-Jun Bahk[2]

[1]College of Earth, Ocean, and Atmospheric Sciences, Oregon State University, 104 CEOAS Administration Bldg, Corvallis, OR 97331, USA

[2]Petroleum and Marine Research Division, Korea Institute of Geosciences and Mineral Resources, 124 Gwahang-no Yuseong-gu, Daejeon 305-350, South Korea

**Abstract**

We present a kinetic model based upon pore water data collected from eight sites drilled during the second Ulleung Basin gas hydrate drilling expedition (UBGH2) in 2010. Three sites were drilled at locations where acoustic chimneys were identified in seismic data, and the rest were drilled on non-chimney (*i.e.* background) environments. Our model, coupled a comprehensive compositional and isotopic data set, is used to illustrate the different biogeochemical processes at play in those two environments, in terms of reactions around the sulfate-methane-transition-zone (SMTZ). Organic matter decomposition is an important process for production of methane, dissolved inorganic carbon (DIC) and consumption of sulfate in the non-chimney sites, whereas anaerobic oxidation of methane (AOM) dominates both carbon and sulfur cycles in the chimney environment. Different sources of methane mediate AOM in the two settings. Internally produced methane through $CO_2$ reduction (CR) and methanogenesis fuels AOM in the non-chimney sites, whereas AOM is sustained by methane from external sources in the chimney sites. We also simulate the system evolution from non-chimney to chimney conditions by increasing the bottom methane supply to a non-chimney setting. We show that the higher $CH_4$ flux leads to a higher microbial activity of AOM, and more organic matter decomposition through methanogenesis. A higher methanogenesis rate and a smaller CR contribution relative to AOM in the chimney sites is responsible for the isotopically light DIC and heavy methane in this environment, relative to the non-chimney sites.

## Introduction

Anaerobic oxidation of methane (AOM) in marine sediments is an effective microbial filter that prevents methane from leaking into the water column and potentially the atmosphere (Barnes and Goldberg, 1976; Heeschen et al., 2005; Chuang et al., 2006; Yang et al., 2006; Reeburgh, 2007; Regnier et al., 2011). A thorough understanding of AOM is thus critical to assessing the role of deep-subseafloor methane (*e.g.*, gas hydrate, gas/oil reservoirs, etc) on the carbon cycle under past, present or future environmental changes. The sulfate-methane-transition-zone (SMTZ) in marine sediments, where sulfate is exhausted and methane concentration starts to increase, is intuitively related to the strength of AOM (Borowski et al., 1996; Dickens, 2001; Chuang et al., 2010); though the actual reaction pathways can not be easily inferred solely from concentration profiles and may require consideration of carbon isotopic data (Borowski et al., 1997; Chatterjee et al., 2011; Hong et al., 2013).

Previous studies have sketched a first-order picture of the many interdependent biogeochemical reactions around the SMTZ (Borowski et al., 1996; Dale et al., 2006; Wallmann et al., 2006; Chatterjee et al., 2011; Regnier et al., 2011; Hong et al., 2013), and it is now widely accepted that the depth of SMTZ is controlled by the interaction of several reactions, such as organoclastic sulfate reduction (Fossing et al., 2000; Wallmann et al., 2006), additional $CO_2$ reduction (Borowski et al., 1997; Pohlman et al., 2008; Hong et al., 2013), and methanogenesis (Chatterjee et al., 2011). To better understand the system, we need a more comprehensive and quantitative understanding of how the carbon and sulfur cycles are connected at this active biogeochemical zone. Hong et al. (2013) presented a box model calculation, based on the balances of mass, flux, and isotopes of carbon, which allows for first-order estimates of the relative weight of these different reactions based on the geochemical profiles in various diffusion-dominated locations. This box model is, however, restricted to steady state conditions and only applicable to environments where diffusion is the dominant mechanism supplying methane to the SMTZ. Seismic surveys in the Ulleung Basin, however, revealed the presence of abundant acoustic chimneys known to act as advective methane gas conduits that fuel massive gas hydrate formation near the seafloor (Haacke et al., 2009; Horozal et al., 2009; Torres et al., 2011; Yoo et al., 2013; Kim et al., 2012; Choi et al., 2013).

In this work, we present a kinetic model that simulates the concentration and isotopic profiles of pore water from eight sites drilled in Ulleung Basin, offshore Korea, during the second gas hydrate drilling expedition (UBGH2) (Figure 1). We build our kinetic model using data from the five sites that are apparently diffusion-dominated, as they were drilled away from seismic blanking structures (non-chimney sites hereafter). These data were used by Hong et al. (2013) in their box model, and permit comparison between the steady state and kinetic model approaches.

We also apply the kinetic model to three additional sites that were drilled at acoustic blanking zones observed on seismic profiles (chimney sites hereafter). Such acoustic blanking zones are indicative to upward migration of free gas through the sediments, which lowers the acoustic velocity, and thus these sites correspond to a high methane flux end member in the Ulleung Basin and elsewhere (Torres et al., 2011; Kim et al., 2012). The very shallow SMTZ (< 3mbsf) and the appearance of massive gas hydrate in shallow sediments (<7 mbsf) is also indicative of a strong methane supply (KIGAM, 2011). We compare carbon and sulfur cycles in these two environments and study the biogeochemical response of the system to an increase of methane flux.

## Model architecture

The model was implemented using CrunchFlow, a FORTRAN routine developed by Steefel (2009), which has been applied to various geochemical simulations (Maher et al., 2009; Yang et al., 2010). The details of model setup, including the full considerations of fundamental parameters and reactions, the geochemical database and input files for CrunchFlow, can be found from the Appendices. A brief introduction is provided below.

### *Model framework*

We chose to model the first 20 meters of sediments at non-chimney sites, since the SMTZ in these settings range from 6.2 to 7.7 mbsf, and within this depth range we have the higher resolution of composition and isotopic data. For chimney sites, we chose to model only the first 5 meters, as the SMTZ here occurs between 1.2 to 2 mbsf and gas hydrate was observed as shallow as ~6 mbsf at site UBGH2-3 and UBGH2-7 (Table A3). Such choice of model frame does not correspond to the extent of methanogenesis, which should exist below our model length (Kim et al., 2011, 2013b; Choi et al., 2013).

We ran the simulation for 400 and 100 kyr at the non-chimney and chimney sites, respectively. These time periods correspond to the time needed for the first sediment parcel to move through the model frame (see Appendix 1 for sedimentation rate considerations). Although steady state is not assumed, the simulation time is long enough for all dissolved and solid species to reach steady state.

We chose 15 primary species as the fundamental building blocks of the model. In addition, we selected ten secondary species, five gases, and five minerals, which can all be formulated exclusively by primary species. The full list of species considered is listed in Table A1 as well as the corresponding reactions in Table A2. We chose Dirichlet-type (*i.e.*, fixed-concentration) upper and lower boundary conditions and assigned them based on the measured concentrations: bottom water composition for the upper boundary and the available measurements nearest to 20 mbsf as the lower boundary. Bottom water composition was used as the initial condition at each site.

*Reaction network*

Our model includes 19 reactions, which are listed in Table A2 with the corresponding abbreviations used in this paper. The reaction network is illustrated in Figure A1, and comprises the carbon (upper middle in Figure A1) and sulfur (lower left in Figure A1) cycles, which are linked via AOM (Eq. A22). Particulate organic matter (POC) is consumed via either sulfate reduction (POCSR) (Eq. A25) or methanogenesis (ME) (Eq. A26). ME implicitly includes both fermentation and $CO_2$ reduction which can be summarized as:

$$\begin{aligned} &2CH_2O + 2H_2O \rightarrow 2CO_2 + 4H_2 \quad \text{(fermentation)} \\ &CO_2 + 4H_2 \rightarrow CH_4 + 2H_2O \quad (CO_2 \text{ reduction}) \end{aligned} \tag{1}$$

Acetoclastic methanogenesis is not considered in our model as previous studies indicate that this metabolic pathway does not contribute significantly to methane generation in marine sediments (Whiticar, 1999; Heuer et al., 2009). Furthermore, the carbon and deuterium isotopes of methane sampled in the Ulleung Basin also demonstrate that $CO_2$ reduction is the primary methane production pathway in this

basin (Choi et al., 2013). Our model includes an additional $CO_2$ reduction reaction (CR, Eq. A23), which is described as methane generated from the dissolved inorganic carbon (DIC) produced primarily from AOM and, to a lesser extent, from ME below SMTZ. This reaction was often overlooked in previous studies (Wallmann et al., 2006; Chatterjee et al., 2011; Chuang et al., 2013). However, Hong et al. (2013) demonstrated its significant role to achieve an isotopic mass balance of carbon around the SMTZ. Authigenic carbonate (CP, Eq. A24) removes dissolved calcium, magnesium and carbonate species from the pore water (Nehza et al., 2012). Methane in our model can be generated in-situ through CR and ME or delivered to our modeled sediment layer by external source, which includes the contribution of methanogenesis below the model frame.

Hydrogen sulfide is produced from both AOM and POCSR. Formation of pyrite (Eq. A27) down to the depth of SMTZ has often been associated with these reactions (*e.g.*, Wallmann et al., 2006; Lim et al., 2011), but the exact formation mechanism remains controversial (Burdige, 2006). For our modeling purposes we assume pyrite precipitation from the less crystalline mineral mackinawite, as has been proposed from both theoretical calculations and lab experiments (Rickard, 1997; Rickard and Luther, 1997, 2007; Dale et al., 2009). This process fixes hydrogen sulfide from pore water and produces hydrogen gas, which supports CR. The most likely iron sources for mackinawite formation are the labile Fe oxyhydroxides. Other minerals, such as hematite may also act as Fe sources. The minerals providing Fe are not considered in the current model.

To correctly account for the change of alkalinity and pH, we included all major cations and anions, as well as various acid-base pairs of carbon, sulfur, nitrogen, and phosphate species (Eq. A11 to A18). The acid-base pairs are treated as secondary species in CrunchFlow, and are assumed to reach immediate equilibrium. $CH_4$ and $CO_2$ gases are allowed to form (Eq. A19 and A20), but for simplicity in this current version of the model, the gas phase is pinned to the pore water; in other words, it is not allowed to migrate as a separate phase and the fluid is assumed to be fully saturated. Kim et al. (2012) presented evidence from carbon isotopic fractionation in support of a two-phase transport (gas and liquid) at chimney sites. We acknowledge this process but have not included this two-phase transport in the current model.

The carbon isotopic profiles were modeled by tracking $^{12}C$ and $^{13}C$ in all carbon species individually. Within our formulation, the measured isotopic variability can be explained by four different processes. First, a diffusion-induced fractionation has been quantified by Zeebe and Wolf-Gladrow (2001), who showed that the diffusion coefficients are inversely proportional to the square root of the reduced masses. Secondly, isotopic changes can result in mixing of carbon with different isotopic signatures and without any isotopic fractionation. For example, DIC released from POCSR (Eq. A25) has a constant carbon isotopic signature that is similar to the organic matter. We used the values of -23 or -19 ‰ reported by Kim (2007) for non-chimney and chimney sites, respectively (see Table A4). ME (Eq. A26) releases methane and DIC with very different isotopic signatures (Table A4) that reflect the isotopic fractionation during this reaction. The authigenic carbonate has a constant carbon isotopic signature of -38‰, and no significant difference in carbon isotopes was observed on authigenic carbonates from chimney and non-chimney sites (Nehza et al., 2012). The third type of isotopic fractionation is the equilibrium reaction between the various carbonate species, which can be as large as 9‰ between $CO_{2(aq)}$ and $HCO_3^-$ (Mook, 1986; Zhang et al., 1995). This is accounted for in our model by including the $^{12}C$ and $^{13}C$ carbonate species. The last source of fractionation comes from the kinetic effect of the non-equilibrium reactions such as AOM and CR. We estimated this fractionation effect by assigning different kinetic constants for each of these reactions as detailed in Appendix 1.

*Model experiment setup*

To investigate how the system responds to an increase in methane diffusional flux, we let the model simulate the changes from the geochemical conditions of UBGH2-1_1 (a non-chimney site) to the conditions observed in UBGH2-3 (a chimney site) by increasing the methane concentration in the bottom boundary condition by a factor of 17, while the concentration of other solutes remained unchanged. Such increase in the bottom boundary condition of methane concentration will result in a higher diffusive flux of methane, which delivers more methane into the model frame during the time length of interest.

**Pore water data and geochemical environment**

The available data allow us to constrain our model results by comparison with measured carbon isotopes of DIC and methane (Figure 2) as well as the concentration of sulfate, calcium, magnesium, ammonium, alkalinity, hydrogen sulfide (only available in 3 sites), and pH (Figure 3). All these data and their corresponding analytic procedures have been reported elsewhere (*e.g.*, Ryu et al., 2012; Choi et al., 2013; Hong et al., 2013; Kim et al., 2013a).

At the non-chimney sites, the depth of SMTZ ranges from 5 to 10 meters below seafloor (mbsf) (Table A3), and gas hydrates occurred disseminated within the sediment or concentrated within coarse layers at depths ranging from ~70-190 mbsf (Table A3), where it occupies 12 to 79% of the pore space (Bahk et al., 2013). In contrast, the shallow depths of the SMTZ (<2 mbsf) at the three chimney sites point to a higher methane flux, which is thought to support formation of massive gas hydrate at shallow depths (<7 mbsf) (Table A3; Torres et al., 2011; Kim et al., 2012; 2013b; Choi et al., 2013).

Distinct geochemical features can be observed from the isotopic profiles between the two groups. There is no significant difference in the isotopic signatures in the deep fluids and gases (>150 mbsf) among all sites (Figure 3 and Table A3). However, around the SMTZ, $\delta^{13}$C-DIC is ~12-20 ‰ lighter at chimney sites relative to the non-chimney sites, while $\delta^{13}$C-$CH_4$ is enriched (~10-15 ‰) in chimney sites. These patterns indicate that reactions around the SMTZ, rather than variations in the fluid source, are responsible for these isotopic patterns.

## Results and Discussion

By fitting our model results to the available data (Figure 3), we are able to derive reaction rate profiles. From these, we calculated the depth-integrated rates in terms of DIC, methane, and hydrogen sulfide production/consumption and reported them in Table 1 and Figure 4. The difference in reaction rates between the non-chimney and chimney sites is discussed in the following paragraphs.

### *DIC cycling around SMTZ*

At all sites, we calculated a $\Delta F_{DIC}$ parameter (Figure 4a), defined as the difference

between inflow and outflow of DIC, a negative value of this parameter represents a net outflux (*i.e.*, DIC outflux > DIC influx). The larger outflux of DIC is due to the permanent low concentration of DIC at seafloor (~2.2 mM), which sustains a concentration gradient between depth of SMTZ and seafloor. The excess of DIC outflux plus the net DIC consumption through reactions (CR and CP) equals to the net DIC production through organic matter degradation (POCSR+ME) and AOM. For all of the non-chimney sites, the DIC production rates through organic matter degradation (POCSR+ME) within the model frame are at least 76% of the $\Delta F_{DIC}$, indicating that the DIC produced through organic matter degradation can account for most of the excess DIC outflux. At these sites, DIC production rate via AOM is always lower than that from organic matter decomposition and accounts for only ~25 to 46% of the total $\Delta F_{DIC}$. On the other hand, at chimney sites, organic matter degradation contributes only slightly to the overall rate, and AOM accounts for more than 85% of the total $\Delta F_{DIC}$.

At non-chimney sites, the primary pathway for organic matter degradation is POCSR, which can account for up to 96% of total organic matter degradation. At chimney sites, however, POCSR within the shallow SMTZ becomes less important. In order to fit the isotopic data at the chimney sites, it is necessary to use higher kinetic constants for ME, which in turn result in higher ME rates in this setting. These results illustrate how the shallow sulfate reduction zone typical of chimney sites in the Ulleung basin (and elsewhere), acts to deliver more labile organic matter to the methanogenesis zone, where high ME rates lead to enhanced methane generation.

CR, the reaction via which methane is produced by reduction of in situ DIC plus that derived from AOM, is an important sink of DIC for all sites (7- 8%). However, the ratio of CR to AOM, which represents the portion of self-supported AOM fueled by the cycling between AOM and CR, is remarkably different between the non-chimney and chimney sites. These ratios range from 19 to 33% at non-chimney sites, but are only <10% at chimney sites. These differences indicate that CR is less important, when AOM is actively fueled by high methane flux.

*$CH_4$ cycling around SMTZ*

Methane produced by organic matter degradation (*i.e.*, ME) within the model frame

supports a fraction of the AOM at all sites (Figure 4b). At the non-chimney sites, up to 35% of methane consumed by AOM comes from ME, whereas a maximum 18% of AOM is supported by ME at chimney sites. Notice that as our model does not include the ME presents beneath the model frame, the rate estimated for ME represents only the contribution within this corresponding depth range and could underestimate the overall contribution. The other internally-produced source of methane, CR, mediates about 19 to 33% of the AOM in the non-chimney sites and less than 10% in the chimney sites. This reaction describes the carbon cycling between AOM and CR, which helps stabilize the SMTZ when the methane flux is low (*i.e.*, non-chimney sites) and becomes less important when methane flux is high (*i.e.*, chimney sites). The methane that is delivered externally fuels only 44 to 63% of AOM in non-chimney sites but becomes much more important (fuels >74% of AOM) at chimney sites.

The externally-delivered methane is the sum of all methane produced below our model frames (*i.e.,* 20 meters in non-chimney sites and 5 meters in chimney sites) regardless of its origin. The source of methane from outside the model frame cannot be directly constrained by our model, but we can make educated inferences based on the assigned boundary conditions. At the chimney sites, the carbon isotopic composition of the methane present at the lower model boundary is similar to that reported for the gas hydrate-bounded methane recovered from the Ulleung Basin (Choi et al., 2013; Kim et al., 2013b), and it is commonly heavier than that for the non-chimney sites (Table A4). However, at all sites the methane isotopic data reflects a microbial source (Choi et al., 2013; Kim et al., 2011, 2012, 2013b), indicating that a large portion of the methane is produced by ME at depths deeper than those defined by our model frames. It is also possible that migration of methane in the free gas phase is responsible for the high methane flux in chimney sites, as suggested by Kim et al. (2012); however the current model does not include a two-phase transport.

If we compare the magnitude of the external methane flux with the SMTZ depth in our sites (Figure 5a), we can observe how the external methane flux increases exponentially as SMTZ depth shoals. Such non-linear relationship was already emphasized by the global dataset of AOM rates relative to the corresponding SMTZ depths compiled by Regnier et al. (2011). If we were to use a linear extrapolation based on the depth of SMTZ at sites UBGH2-5 and UBGH2-7 and assume that AOM is totally fueled by

external methane, we would predict the external methane flux at site UBGH2-7 to be only four times higher than that at site UBGH2-5. A better estimate based on our model shows that the methane flux at site UBGH2-7 is ~10 times higher than that at site UBGH2-5.

From Figure 5b, a loosely proportional relationship between external methane flux and the thickness of gas hydrate occurrence zone (GHOZ; BSR depth minus depth of first gas hydrate observed) suggests that the thickness of gas hydrate reservoir may indeed influence the external methane flux. However, using the strength of external flux to infer the thickness of GHOZ may be problematic as factors such as lithology also influence the abundance and the type of gas hydrate reservoir in Ulleung Basin (Bahk et al, 2013) and elsewhere (Torres et al., 2008). A universal relationship between geochemical- or geophysical-defined boundaries (*e.g.*, SMTZ, BSR, or GHOZ) and external methane fluxes as proposed by Bhatnagar et al. (2008) maybe possible, but to fully constrain this possibility will require more data.

*Sulfur cycling around SMTZ*

The entire sulfate flux into the sediments from the overlying seawater is converted to hydrogen sulfide by either POCSR or AOM within the model frame (Figure 4c). For the non-chimney sites, POCSR accounts for 40 to 65% of the total sulfate reduction but only less than 8% is consumed by POCSR in the chimney sites. Our model suggests a rapid hydrogen sulfide turnover rate, since the pore water hydrogen sulfide content predicted by the model is low (Figure 3). Most of the pore water sulfide is sequestered in the solid phase through pyrite and mackinawite formation (Figure 2). Our model estimates that sulfide mineral formation (pyrite plus mackinawite) is responsible for a 2 to 5 wt% increase of sulfur-containing minerals (Figure 6). A full inventory of the sulfur-phase partitioning in the Ulleung Basin is not available, however, a first order mass balance of sulfur species both in pore water and solid phases is illustrated by comparing the measured profiles of the relevant species (*i.e.*, sulfate and sulfide in pore water as well as total sulfur from sediments) with our model results from two non-chimney sites (UBGH2-1_1 and UBGH2-10) and one chimney site (UBGH2-7) where data are available (Figure 6).

The model reproduces the observed low hydrogen sulfide concentration in the pore

water (Figure 6). The pyrite content estimated for these three sites is usually half of the measured total sulfur (TS) content in the sediments (KIGAM, 2011). By including the model-estimated mackinawite content, the observed level of TS in the sediments can be better accounted for. The SEM photos (Kim, unpublished data) in Figure 6d shows the framboidal pyrite observed below SMTZ in UBGH2-1_1 which has been attributed to authigenic processes (Wilkin, 1997; Butler and Rickard, 2000; Campbell et al., 2002; Park et al., 2005).

Admittedly, our current model includes only a basic consideration of the sulfur cycle but the pyrite formation mechanism considered here is one of the three potential pathways for pyrite formation (see Rickard and Luther (2007) for reviews). Butler and Rickard (2000) successfully synthesized framboidal pyrite from mackinawite and dissolved hydrogen sulfide, and we use their results as a basis for the proposed mechanism operational in the Ulleung Basin. However, more work is clearly needed both in terms of analytical efforts to partition the sulfur species in the Ulleung Basin and an associated model development to investigate the reaction network between carbon and sulfur cycles in marine sediments. Nevertheless, the first-order agreement between modeled and observed profiles in both solid and pore water phases (Figure 6) suggests a satisfactory mass balance of sulfur species, as well as a reasonable estimate of sulfide turnover rate (*i.e.*, from dissolved phase to solid phase). The sequestration of sulfide from pore water into solid phase proposed here supplies the hydrogen gas required in CR, which is essential to achieve carbon isotopic mass balance.

*The significance of CR around SMTZ*

AOM has been long identified as the solo connection between dissolved methane and carbonate species in pore water. In our study, however, we emphasize $CO_2$ reduction as a reverse connection that counteracts the effect of AOM. Our previous effort (Hong et al., 2013) and other studies (Borowski et al., 1997; Pohlman et al., 2008) have demonstrated the need to include $CO_2$ reduction to satisfy isotopic mass balance of carbon. In this work, in addition to the balance in mass and isotope budgets of dissolved carbon species (*i.e.*, DIC and methane), we also account for the dissolved hydrogen source required in $CO_2$ reduction via pyrite formation (Figure 6 and Table 1). The satisfactory agreement of sulfur species profiles in two non-chimney sites and one chimney sites (Figure 6), indicate that the pyrite formation rates derived from our

model are reasonable, and furthermore, mass balances in carbon and sulfur cycling supports the proposed reaction network, which includes the additional $CO_2$ reduction within the SMTZ as a significant component of the carbon cycle in this biogeochemically active zone.

At non-chimney sites, the dissolved hydrogen gas production rate (*i.e.*, pyrite formation) is less than 7 μmol/cm$^2$/yr. This value is within10% of the estimated hydrogen gas consumption rate through CR (*i.e.*, 4 times of CR rate in Table 1 due to the stoichiometry in Eq. A23), and indicates a rapid turnover rate in non-chimney sites. In contrast, there is a significant imbalance between production and consumption of dissolved hydrogen gas at the three chimney sites: production rates are generally twice as large as consumption rates. Pyrite formation in chimney sites is strongly stimulated by the rapid AOM rates fueled by the enhanced bottom methane flux in the chimney sites. CR is also stimulated by the enhanced AOM in the chimney sites (Table 1) but not to the degree of pyrite formation since CR is inhibited by the presence of sulfate above SMTZ. As mass balance is strictly satisfied in the model, the difference between production and consumption rates is accounted by diffusional lost of dissolved hydrogen to seafloor and bottom of the model frame.

*Model experiment result*

To develop an understanding of the change that a system experiences when subjected to an increase in bottom methane supply, we allowed our model to evolve from the concentration and isotopic profiles currently observed at non-chimney site UBGH2-1_1, to the conditions observed at the chimney site UBGH2-3. In addition to the increase in bottom methane supply, to simulate the conditions at chimney locations (Figure 7a to 7c), two other modifications are required to accurately match the pore water suite observed at the high methane flux environment. First, the simulation necessitates a larger AOM kinetic constant, which indicates that at high methane flux sites there is a higher microbial activity. Second, when there is more methane delivered externally to the system, more organic matter is subject to the degradation through ME rather than POCSR, due to the shoaling of the SMTZ.

If only the strength of external methane source is increased, the AOM rate calculated

for the non-chimney sites is not able to keep up with the flux of methane from the bottom supply, and the model will yield the erroneous result of a high methane concentration in the sulfate reduction zone. With a higher AOM kinetic constant methane is now exhausted in the sulfate reduction zone at a faster rate, and SMTZ becomes shallower. The predicted increase in AOM rate by 2-orders-of-magnitude (Figure 7d and 7e) is in agreement with the higher concentration of methyl coenzyme M reductase (mcrA) observed at chimney sites relative to the non-chimney sites (KIGAM, 2011; Choi et al., 2013). Wegener and Boetius (2009), who studied the response of AOM strength to changes in methane flux in a flow-through simulator, also observed a timely increase in AOM rate in response to an increase of methane supply.

If only a high AOM rate fueled by the high methane flux is considered, the pH and carbon isotopes resulting from this enhanced reaction rate will not match our observations. A good fit to the data is obtained by increasing the decomposition rate of organic matter through ME rather than POCSR (Figure 7f). Collectively, these changes (lower CR to AOM ratios and higher ME rates), are responsible for the isotopically light DIC and heavy methane observed in the SMTZ region of the chimney sites, relative to the non-chimney sites (Figure 2).

An increase in organic matter decomposition via ME is consistent with the fact that a shallow sulfate reduction zone will limit the extent of POCSR, since the organic matter will not spend enough time in that redox zone before burial in sediments devoid of sulfate, where it is then available for ME. This effect is further enhanced because the newly-deposited organic matter is more labile than older more-degraded organic carbon. Thus by limiting the time the organic matter resides in the sulfate-bearing zone, there is an increase in both the total amount as well as in the labile fraction of organic matter available for methane production in shallow (<10 mbsf) sediments. This effect has not been considered in current global methane hydrate inventories based on methane generation potential of continental margin sediments (Burwicz et al., 2011; Wallmann et al., 2012; Pinero et al., 2013) and should be considered in future global assessments.

The change in degradation mode intuitively suggests a positive feedback in high methane flux systems. However, due to the different response time between the

dissolved and solid phases, such positive feedback is limited. As the external methane flux is enhanced, driven by changes in state of the deep gas reservoirs (*e.g.*, gas hydrate, pore pressure, seismicity etc), the SMTZ rapidly migrates upwards and adjusts itself to a new position, determined by the strength of the external methane flux. Such adjustment is complete in couple thousand years (2 kyr in our model simulation), depending on the attendant sedimentation rate (*i.e.*, less time required if sedimentation is higher). With the sedimentation rate ($5.6\times10^{-5}$ m/yr) assigned in our model, only ~10 cm of sediments will be buried during this time. However, due to the shoaling of SMTZ, more sediment is now exposed to the attack by ME. The carbon isotopic data and pH will begin to reflect the increase in ME rate after 2 kyr. The depth of SMTZ also slightly decreases in this stage (~10 cm). Due to the lower ME rate relative to the AOM rate, it takes in the order of $10^4$ years (50 kyr in our model simulation) for the system to reach steady state.

**Conclusions**

Our kinetic model can successfully reproduce the compositional and isotopic profiles observed at the eight UBGH2 drilled sites. Striking differences in the biogeochemical processes between the chimney and non-chimney environment were revealed and illustrated in Figure 8. As a result of the study, we conclude the following:

1. Organic matter that is buried in a non-chimney environment is degraded in the 6-8 m thick sulfate reduction zone through POCSR, and is responsible for the majority of the DIC production in the pore water. This process consumes 40-65% of the sulfate inflow from the seafloor while the rest of sulfate reacts with the methane from beneath the SMTZ. 19-33% of the AOM is mediated by the methane produced internally through $CO_2$ reduction in non-chimney environments, which utilizes hydrogen gas produced from pyrite formation. Methane produced by organic matter degradation through ME can also account for 8.2 -35% of the AOM rate. External methane pool contributes less than 65% of the total AOM rate in all non-chimney sites.

2. In contrast, the strong external methane inflow dominates the consumption of sulfate and production of DIC through AOM in the chimney sites. Organic matter

degradation becomes less important. While most (80~98%) of the organic matter is degraded through POCSR in the non-chimney sites (comparing the contributions from ME and POCSR in Figure 4a), more organic matter (35~100%) is now degraded through ME at the chimney sites due to the shrink of sulfate reduction zone (*i.e.*, shoaling of SMTZ). This change in organic matter degradation modes and the resulting increase in methane production potential should be considered in the future assessment of global gas hydrate inventories.

3. Although the consideration of sulfur cycle in our model is still pre-matured, our model can, to a first order, account for the mass balance of several sulfur and carbon species in both pore water and solid phases. Such results infer the necessity and likelihood of an additional $CO_2$ reduction (CR), which utilizes the hydrogen gas produced from pyrite formation. The reactions proposed serve as a novel link, other than AOM, between carbon and sulfur cycles in the marine sediments.

4. Our model experiment demonstrates that the evolution from a non-chimney site to a chimney site requires both a higher bottom methane supply and higher AOM microbial activity. Pathway of organic matter degradation changes in response to the shoaling of SMTZ: more organic matter is degraded through ME than POCSR.

5. From our model assessment, we conclude that the different carbon isotopic signatures observed around SMTZ in high and low methane flux conditions is the result of a lower CR to AOM rate ratio and a higher ME reactivity in sites experiencing a higher methane flux.

**Acknowledgements**

This project was made possible with the funding support from US Department of Energy, contract numbers: DE-FE0004000 and DOE Award No.: DE-FE0010496. In addition we acknowledge support from Korea Institute of Geosciences and Mineral Resources (KIGAM) (GP2012-026) and the Hanse-Wissenschaftskolleg, Institute for Advanced Study in Delmenhorst, Germany through a fellowship to MT. The authors would like to thank Dr. Robert Harris, Dr. Clare Reimers, and two anonymous

503 reviewers for the insightful comments help shaping this manuscript.
504

**Figure Captions**

Figure 1: Map of the eight sites drilled during the 2010 Ulleung Basin gas hydrate drilling expedition (UBGH2) used in this study. The three sites drilled on acoustic chimneys (Torres et al., 2011) were plotted in red triangles.

Figure 2: Carbon isotopic profiles of dissolved inorganic carbon (DIC) and methane. (a) DIC carbon isotopes from all eight sites investigated. Detailed DIC isotope profiles in the upper 25 meters are plotted in (b) and (c) for chimney (blue) and non-chimney (green) sites, respectively. (d) Methane carbon isotopes in the void and headspace gas samples from all sites (blue symbols: chimney sites; green symbols: non-chimney sites). (e) The methane carbon isotope for the first 25 m. These DIC and methane carbon isotopic profiles suggest that the fluid source (> 150 mbsf) is not noticeably different in terms of the carbon isotopic signature at all sites. It is the reactions around the SMTZ that cause the observed variation.

Figure 3: Model results for (a) the five non-chimney sites and (b) the three chimney sites, showing good fit to pore water composition and isotopic profiles.

Figure 4: Depth-integrated rates estimated from our kinetic model at all sites. Note the different scales between the non-chimney (upper 5 panels) and chimney (lower 3 panels) sites. (a) Rates of the five DIC production/consumption reactions and their percentages relative to the $\Delta F_{dic}$, defined as the flux difference of input and output DIC (negative values represent net outflux). (b) Rates of the three methane sources and their percentages relative to AOM rate. (c) Rates of the four hydrogen sulfide production/consumption reactions and their percentage relative to total hydrogen sulfide production rate (or total sulfate reduction rate, total sulfate influx from seafloor). The very different carbon and sulfur cycles between the chimney and non-chimney sites are apparent from this comparison. See text for details.

Figure 5: Correlations between external methane flux and (a) SMTZ depth and (b) thickness of gas hydrate occurrence zone (GHOZ). Thickness of GHOZ is calculated from the difference between depths of BSR and first gas hydrate occurrence listed in Table A3. The non-linearity in both plots suggests that both the depth of the SMTZ and

the thickness of the GHOZ are not solely dependant on the magnitude of an external methane flux. Other factors or processes are may be of the same importance.

Figure 6: Profiles of pore water sulfate, sulfide, and sedimentary total sulfur (TS). (a)-(c) Results from two non-chimney sites (UBGH2-1_1 and UBGH2-10) and one chimney site (UBGH2-7) were shown. The TS data are from KIGAM (2011). The agreement between modeled and observed profiles suggests that our model can satisfactory account for the mass balance of different sulfur species. The resulting hydrogen production rate from pyrite formation estimated from our model is therefore reasonable and could sustain the CR rate required to fulfill the isotopic mass balance of carbon. (d) SEM photos of the framboidal pyrite observed from UBGH2-1_1 at 13.45 mbsf (Kim, unpublished) which suggests the authigenic origin of pyrite.

Figure 7: Evolution of a system from a low methane flux (red: non-chimney site UHGH2-1_1) to one of high methane flux (blue: chimney site UBGH2-3). In response to an increase in bottom methane supply (17 times larger), the AOM and CR rates increase by two orders of magnitude (note change in x axis scale), but the fraction of AOM fueled by CR drops from 30% in the initial low flux condition to 10% in the final high flux condition. POCSR is the primary organic matter degradation pathway in the initial low flux condition while more organic matter is degraded through ME in the final condition. This change in degradation pathways is related to the shoaling of SMTZ driven by an increase in bottom methane supply and it is an important consideration in estimates of methane-generation potential in marine sediments.

Figure 8: Cartoon illustrates the different modes of carbon cycling around SMTZ in the (a) non-chimney and (b) chimney environments in the Ulleung Basin. Size of the arrows represents the strength of fluxes or rates. See text for details.

567 **References**

568 Bahk JJ, Kim G-Y, Chun JH, Lee JY, Ryu BJ, Lee J-H, Son B-K & Collett TS (2013)
569 Characterization of gas hydrate reservoirs in the Ulleung Basin, East Sea (Korea),
570 by integration of core and log data. Marine and Petroleum Geology, 47: 30-42.
571 Barnes RO & Goldberg ED (1976) Methane production and consumption in anoxic
572 marine-sediments. Geology 4: 297-300.
573 Bhatnagar G, Chapman WG, Dickens GR, Dugan B & Hirasaki GJ (2008)
574 Sulfate-methane transition as a proxy for average methane hydrate saturation in
575 marine sediments. Geophysical Research Letters 35, L03611,
576 doi:10.1029/2007GL032500.
577 Borowski WS, Paull CK & Ussler W (1996) Marine pore-water sulfate profiles indicate
578 in situ methane flux from underlying gas hydrate. Geology 24: 655-658.
579 Borowski WS, Paull CK & Ussler W (1997) Carbon cycling within the upper
580 methanogenic zone of continental rise sediments: An example from the
581 methane-rich sediments overlying the Blake Ridge gas hydrate deposits. Marine
582 Chemistry 57: 299-311.
583 Burdige DJ (2006) Geochemistry of marine sediments. Princeton University Press ,
584 Princeton New Jersey.
585 Burwicz EB, Ruepke LH & Wallmann K (2011) Estimation of the global amount of
586 submarine gas hydrates formed via microbial methane formation based on
587 numerical reaction-transport modeling and a novel parameterization of Holocene
588 sedimentation. Geochim. Cosmochim. Acta 75: 4562-4576
589 Butler IB & Rickard D (2000) Framboidal pyrite formation via the oxidation of iron (II)
590 monosulfide by hydrogen sulphide. Geochim. Cosmochim. Acta 64: 2665-2672
591 Campbell KA, Farmer JD & Des Marais D (2002) Ancient hydrocarbon seeps from the
592 Mesozoic convergent margin of California: carbonate geochemistry, fluids and
593 palaeoenvironments. Geofluids 2: 63-94
594 Chatterjee S, Dickens GR, Bhatnagar G, Chapman WG, Dugan B, Snyder GT &
595 Hirasaki GJ (2011) Pore water sulfate, alkalinity, and carbon isotope profiles in
596 shallow sediment above marine gas hydrate systems: A numerical modeling
597 perspective. Journal of Geophysical Research-Solid Earth 116, B09103, doi:
598 10.1029/2011JB008290.
599 Choi J, Kim J-H, Torres ME, Hong W-L, Lee J-W, Yi BY, Bahk JJ & Lee K-E (2013)
600 Gas origin and migration in the Ulleung Basin, East Sea; results from the Second

601 Ulleung Basin Gas Hydrate Drilling Expedition (UBGH2). Marine and
602 Petroleum Geology, 47: 113-124.
603 Chuang PC, Dale AW, Wallmann K, Haeckel M, Yang TF, Chen NC, Chen HC, Chen
604 HW, Lin S, Sun CH, You CF, Horng CS, Wang YS & Chung SH (2013) Relating
605 sulfate and methane dynamics to geology: Accretionary prism offshore SW
606 Taiwan. Geochemistry Geophysics Geosystems 14: 2523-2545
607 Chuang PC, Yang TF, Hong WL, Lin S, Sun CH, Lin ATS, Chen JC, Wang Y & Chung
608 SH (2010) Estimation of methane flux offshore SW Taiwan and the influence of
609 tectonics on gas hydrate accumulation. Geofluids 10: 497-510.
610 Chuang PC, Yang TF, Lin S, Lee HF, Lan TFF, Hong WL, Liu CS, Chen JC & Wang Y
611 (2006) Extremely high methane concentration in bottom water and cored
612 sediments from offshore southwestern Taiwan. Terrestrial Atmospheric and
613 Oceanic Sciences 17: 903-920.
614 Dale AW, Bruchert V, Alperin M & Regnier P (2009) An integrated sulfur isotope
615 model for Namibian shelf sediments. Geochimica et Cosmochimica Acta 73:
616 1924-1944.
617 Dale AW, Regnier P & Van Cappellen P (2006) Bioenergetic controls on anaerobic
618 oxidation of methane (AOM) in coastal marine sediments: A theoretical analysis.
619 American Journal of Science 306: 246-294.
620 Dickens GR (2001) Sulfate profiles and barium fronts in sediment on the Blake Ridge:
621 Present and past methane fluxes through a large gas hydrate reservoir.
622 Geochimica et Cosmochimica Acta 65: 529-543.
623 Fossing H, Ferdelman TG & Berg P (2000) Sulfate reduction and methane oxidation in
624 continental margin sediments influenced by irrigation (South-East Atlantic off
625 Namibia). Geochimica et Cosmochimica Acta 64: 897-910.
626 Haacke RR, Hyndman RD, Park KP, Yoo DG, Stoian I & Schmidt U (2009) Migration
627 and venting of deep gases into the ocean through hydrate-choked chimneys
628 offshore Korea. Geology 37: 531-534.
629 Heeschen KU, Collier RW, de Angelis MA, Suess E, Rehder G, Linke P &
630 Klinkhammer GP (2005) Methane sources, distributions, and fluxes from cold
631 vent sites at Hydrate Ridge, Cascadia Margin. Global Biogeochemical Cycles 19,
632 GB2016, doi:10.1029/2004GB002266.
633 Heuer VB, Pohlman JW, Torres ME, Elvert M & Hinrichs K-U (2009) The stable
634 carbon isotope biogeochemistry of acetate and other dissolved carbon species in

635 deep subseafloor sediments at the northern Cascadia Margin. Geochim.
636 Cosmochim. Acta 73: 3323-3336
637 Hong W-L, Torres ME, Kim J-H, Choi J & Bahk J-J (2013) Carbon cycling within the
638 sulfate-methane-transition-zone in marine sediments from the Ulleung Basin.
639 Biogeochemistry: 1-20.
640 Horozal S, Lee GH, Yi BY, Yoo DG, Park KP, Lee HY, Kim W, Kim HJ & Lee K
641 (2009) Seismic indicators of gas hydrate and associated gas in the Ulleung Basin,
642 East Sea (Japan Sea) and implications of heat flows derived from depths of the
643 bottom-simulating reflector. Marine Geology 258: 126-138.
644 KIGAM (2011) Studies on Gas Hydrate Geology and Geochemistry. KIGAM research
645 report (p 951). Daejeon.
646 Kim J-H (2007) Geochemical Characteristic of Organic Matter, Pore Waters and
647 Methane Gas of Upper Quaternary Sediments from the Ulleung Basin, East Sea.
648 Seoul National University, Seoul
649 Kim J-H, Park MH, Chun JH & Lee JY (2011) Molecular and isotopic signatures in
650 sediments and gas hydrate of the central/southwestern Ulleung Basin: high
651 alkalinity escape fuelled by biogenically sourced methane. Geo-Marine Letters
652 31: 37-49.
653 Kim J-H, Torres ME, Choi J, Bahk JJ, Park MH & Hong WL (2012) Inferences on gas
654 transport based on molecular and isotopic signatures of gases at acoustic
655 chimneys and background sites in the Ulleung Basin. Organic Geochemistry 43:
656 26-38.
657 Kim J-H, Torres ME, Hong W-L, Choi J, Riedel M, Bahk JJ & Kim S-H (2013a) Pore
658 fluid chemistry from the Second Gas Hydrate Drilling Expedition in the Ulleung
659 Basin (UBGH2): Source, mechanisms and consequences of fluid freshening in
660 the central part of the Ulleung Basin, East Sea. Marine and Petroleum Geology,
661 47: 99-112.
662 Kim J-H, Torres ME, Lee JY, Hong W-L, Holland M, Park M-H, Choi J & Kim G-Y
663 (2013b) Depressurization experiment of pressure cores from the central Ulleung
664 Basin, East Sea; insights into gas chemistry. Organic Geochemistr, 62: 86-95.
665 Lim YC, Lin S, Yang TF, Chen YG & Liu CS (2011) Variations of methane induced
666 pyrite formation in the accretionary wedge sediments offshore southwestern
667 Taiwan. Marine and Petroleum Geology 28: 1829-1837.
668 Maher K, Steefel CI, White AF & Stonestrom DA (2009) The role of reaction affinity

669 and secondary minerals in regulating chemical weathering rates at the Santa Cruz
670 Soil Chronosequence, California. Geochimica et Cosmochimica Acta 73:
671 2804-2831.
672 Mook WG (1986) C-13 in a atmospheric $CO_2$. Netherlands Journal of Sea Research 20:
673 211-223.
674 Nehza O, Woo KS, Chun J-H, Bahk J-J, Kim JK & Hyun S (2012) The origin of
675 cold-water authigenic carbonates from deep-water, muddy sediments in the
676 Ulleung Basin, East Sea of Korea. Geosciences Journal 16: 25-34.
677 Park MH, Kim JH, Kim IS, Ryu BJ & Yu KM (2005) Tephrostratigraphy and
678 paleo-environmental implications of Late Quaternary sediments and interstitial
679 water in the western Ulleung Basin, East/Japan Sea. Geo-Marine Letters 25:
680 54-62.
681 Pinero E, Marquardt M, Hensen C, Haeckel M & Wallmann K (2013) Estimation of the
682 global inventory of methane hydrates in marine sediments using transfer
683 functions. Biogeosciences 10: 959-975
684 Pohlman JW, Ruppel C, Hutchinson DR, Downer R & Coffin RB (2008) Assessing
685 sulfate reduction and methane cycling in a high salinity pore water system in the
686 northern Gulf of Mexico. Marine and Petroleum Geology 25: 942-951.
687 Reeburgh WS (2007) Oceanic methane biogeochemistry. Chemical Reviews 107:
688 486-513.
689 Regnier P, Dale AW, Arndt S, LaRowe DE, Mogollon J & Van Cappellen P (2011)
690 Quantitative analysis of anaerobic oxidation of methane (AOM) in marine
691 sediments: A modeling perspective. Earth-Science Reviews 106: 105-130
692 Rickard D (1997) Kinetics of pyrite formation by the H2S oxidation of iron (II)
693 monosulfide in aqueous solutions between 25 and 125 degrees C: The rate
694 equation. Geochim. Cosmochim. Acta 61: 115-134.
695 Rickard D & Luther GW (1997) Kinetics of pyrite formation by the H2S oxidation of
696 iron(II) monosulfide in aqueous solutions between 25 and 125 degrees C: The
697 mechanism. Geochimica et Cosmochimica Acta 61: 135-147.
698 Rickard D & Luther GW (2007) Chemistry of iron sulfides. Chemical Reviews 107:
699 514-562.
700 Ryu B-J, Kim GY, Chun JH, Bahk JJ, Lee JY, Kim J-H, Yoo DG, Collett TS, Riedel M,
701 Torres ME, Lee S-R & UBGH2 S (2012) Ulleung Basin Gas Hydrate Drilling
702 Expedition 2 (UBGH2). Expedition Report (p 667). KIGAM, Daejeon.

703 Steefel CI (2009) CrunchFlow- Software for Modeling Multicomponent Reactive Flow
704 and Transport: User's Manual, pp 91.
705 Torres ME, Kim J-H, Choi J-Y, Ryu B-J, Bahk J-J, Riedel M, Collett T, Hong W-L &
706 Kastner M (2011) Occurrence of High Salinity Fluids Associated with Massive
707 Near-seafloor Gas Hydrate Deposits. 7th International Conference on Gas
708 Hydrates, Edinburgh, Scotland, United Kingdom.
709 Torres ME, Trehu AM, Cespedes N, Kastner M, Wortmann UG, Kim JH, Long P,
710 Malinverno A, Pohlman JW, Riedel M & Collett T (2008) Methane hydrate
711 formation in turbidite sediments of northern Cascadia, IODP Expedition 311.
712 Earth Planet. Sci. Lett. 271: 170-180.
713 Wallmann K, Aloisi G, Haeckel M, Obzhirov A, Pavlova G & Tishchenko P (2006)
714 Kinetics of organic matter degradation, microbial methane generation, and gas
715 hydrate formation in anoxic marine sediments. Geochimica et Cosmochimica
716 Acta 70: 3905-3927.
717 Wallmann K, Pinero E, Burwicz E, Haeckel M, Hensen C, Dale A & Ruepke L (2012)
718 The Global Inventory of Methane Hydrate in Marine Sediments: A Theoretical
719 Approach. Energies 5: 2449-2498
720 Wegener G & Boetius A (2009) An experimental study on short-term changes in the
721 anaerobic oxidation of methane in response to varying methane and sulfate fluxes.
722 Biogeosciences 6: 867-876.
723 Whiticar MJ (1999) Carbon and hydrogen isotope systematics of bacterial formation
724 and oxidation of methane. Chem. Geol. 161: 291-314.
725 Yang L, Steefel CI, Marcus MA & Bargar JR (2010) Kinetics of Fe(II)-Catalyzed
726 Transformation of 6-line Ferrihydrite under Anaerobic Flow Conditions.
727 Environmental Science & Technology 44: 5469-5475.
728 Yang TF, Chuang PC, Lin S, Chen JC, Wang Y & Chung SH (2006) Methane venting
729 in gas hydrate potential area offshore of SW Taiwan: Evidence of gas analysis of
730 water column samples. Terrestrial Atmospheric and Oceanic Sciences 17:
731 933-950.
732 Yoo DG, Kang NK, Yi BY, Kim GY, Ryu BJ, Lee K, Lee GH & Riedel M (2013)
733 Occurrence and seismic characteristics of gas hydrate in the Ulleung Basin, East
734 Sea. Marine and Petroleum Geology, 47: 236-247.
735 Zeebe RE & Wolf-Gladrow D (2001) $CO_2$ in Seawater Equilibrium, Kinetics, Isotopes.
736 Elsevier Oceanography Series, Vol. 65, Elsevier Science, New York.

737 Zhang J, Quay PD & Wilbur DO (1995) Carbon-isotope fractionation during gas-water
738 exchange and dissolution of $CO_2$. Geochimica et Cosmochimica Acta 59:
739 107-114.

740

**Table1**

Table 1: Depth integrated rates for all study sites

(A) μmol DIC/$cm^2$ porous medium/yr

| | UBGH2-1_1 | UBGH2-2_1 | UBGH2-5 | UBGH2-6 | UBGH2-10 | UBGH2-3 | UBGH2-7 | UBGH2-11 |
|---|---|---|---|---|---|---|---|---|
| Cal-Ca | -0.9 | -0.9 | -0.6 | -0.7 | -1.6 | -0.3 | -0.2 | -0.5 |
| Cal-Mg | -1.0 | -1.5 | -1.3 | -0.4 | -1.0 | -0.3 | -0.2 | -0.4 |
| POCSR | 14.9 | 11.9 | 14.8 | 11.1 | 18.5 | 0.1 | 5.2 | 4.6 |
| ME | 0.3 | 2.9 | 0.4 | 2.2 | 0.5 | 10.7 | 2.9 | 6.0 |
| AOM | 4.0 | 9.0 | 4.0 | 6.4 | 5.5 | 58.8 | 28.3 | 58.9 |
| CR | -1.3 | -1.7 | -1.1 | -1.4 | -1.6 | -4.9 | -2.7 | -4.1 |
| DIC flux | -16.1 | -19.6 | -16.3 | -17.2 | -20.3 | -64.1 | -33.4 | -64.5 |

(B) μmol $CH_4$/$cm^2$ porous medium/yr

| | UBGH2-1_1 | UBGH2-2_1 | UBGH2-5 | UBGH2-6 | UBGH2-10 | UBGH2-3 | UBGH2-7 | UBGH2-11 |
|---|---|---|---|---|---|---|---|---|
| ME | 0.3 | 2.9 | 0.4 | 2.2 | 0.5 | 10.7 | 2.9 | 6.0 |
| AOM | -4.0 | -9.0 | -4.0 | -6.4 | -5.5 | -58.8 | -28.3 | -58.9 |
| CR | 1.3 | 1.7 | 1.1 | 1.4 | 1.6 | 4.9 | 2.7 | 4.1 |
| $CH_4$ flux | 2.4 | 4.3 | 2.5 | 2.8 | 3.4 | 43.2 | 22.7 | 48.7 |

(C) μmol $HS^-$/$cm^2$ porous medium/yr

| | UBGH2-1_1 | UBGH2-2_1 | UBGH2-5 | UBGH2-6 | UBGH2-10 | UBGH2-3 | UBGH2-7 | UBGH2-11 |
|---|---|---|---|---|---|---|---|---|
| Pyrite | -4.9 | -6.1 | -5.2 | -5.0 | -6.5 | -37.9 | -20.1 | -44.6 |
| Mack | -7.4 | -8.8 | -6.2 | -7.0 | -8.3 | -20.9 | -10.8 | -16.6 |
| POCSR | 7.5 | 5.9 | 7.4 | 5.6 | 9.3 | 0.1 | 2.6 | 2.3 |
| AOM | 4.0 | 9.0 | 4.0 | 6.4 | 5.5 | 58.8 | 28.3 | 58.9 |
| Tot $SO_4$ reduction | 11.5 | 14.9 | 11.4 | 12.0 | 14.7 | 58.9 | 31.0 | 61.2 |

Fig1

Click here to download high resolution image

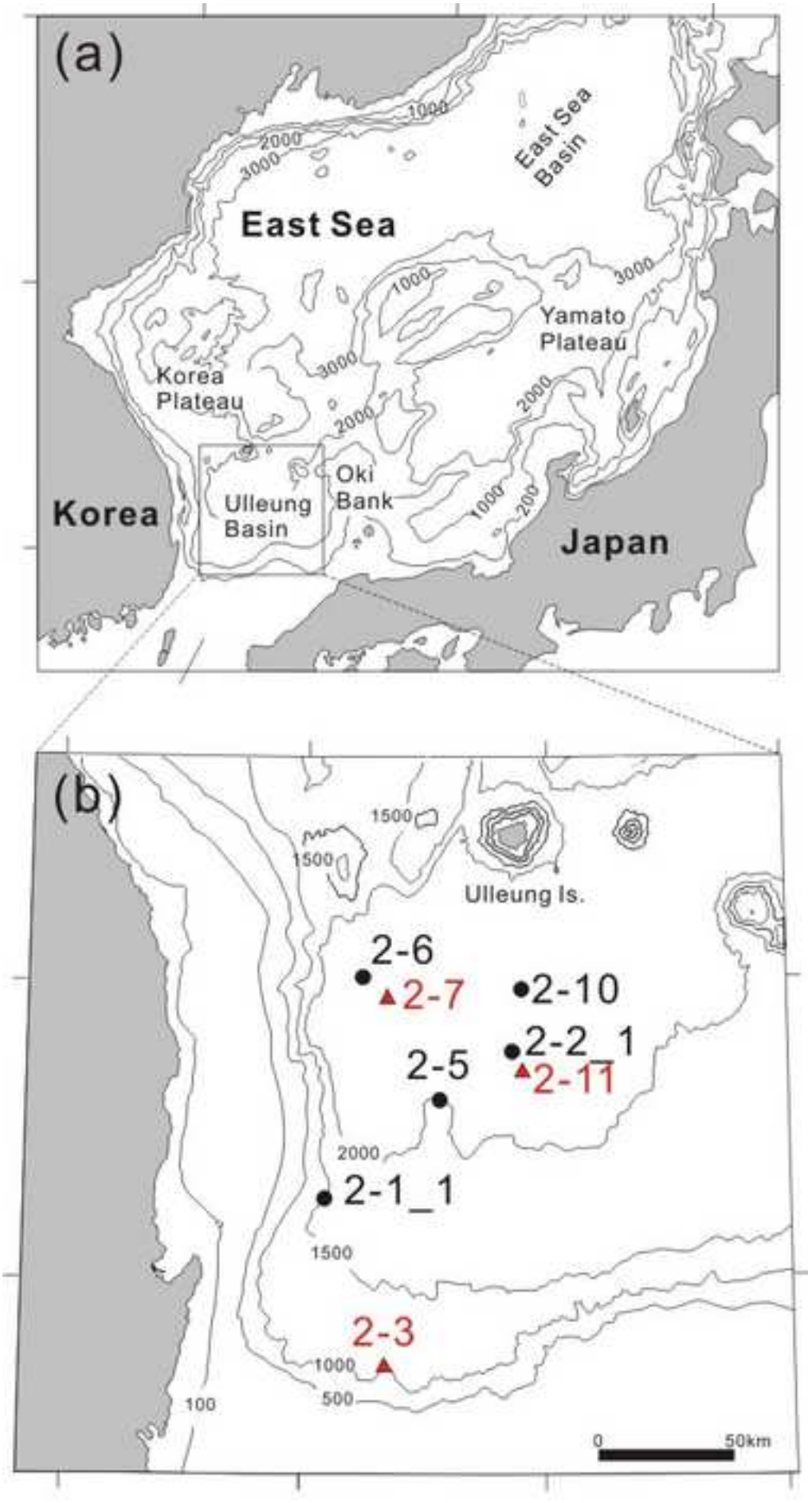

Fig2

Click here to download high resolution image

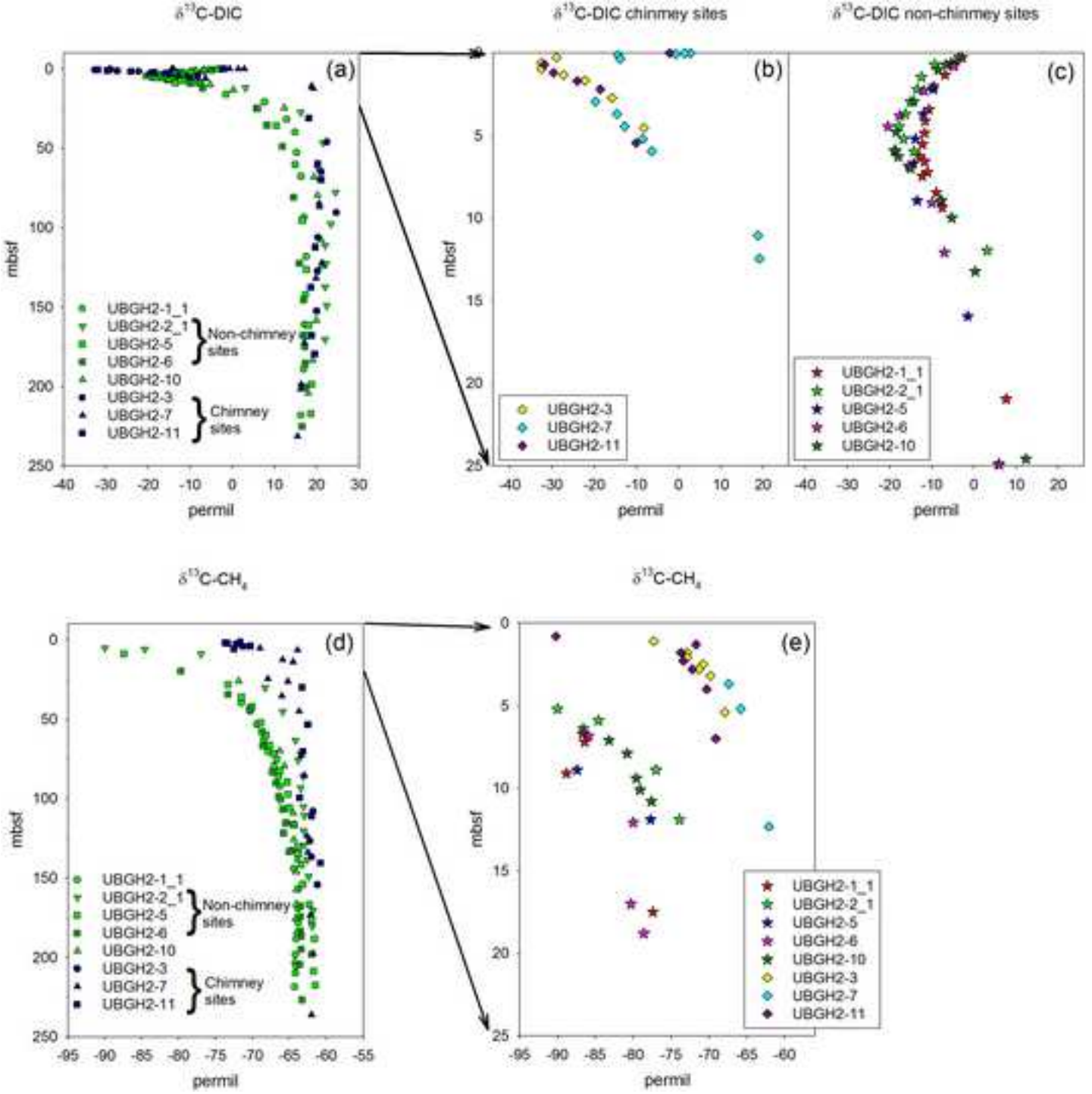

**Fig3a**

**Click here to download high resolution image**

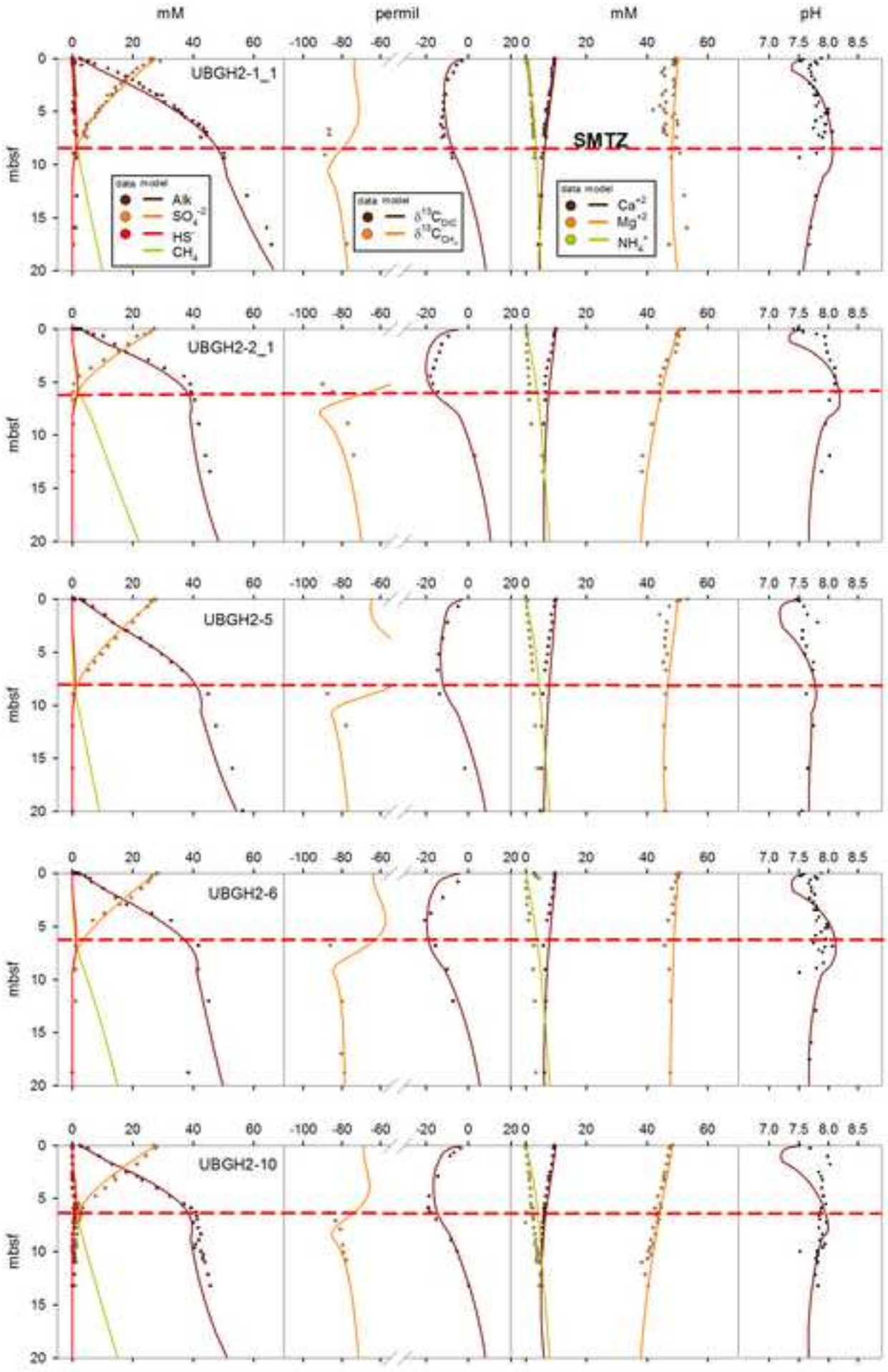

**Fig3b**

**Click here to download high resolution image**

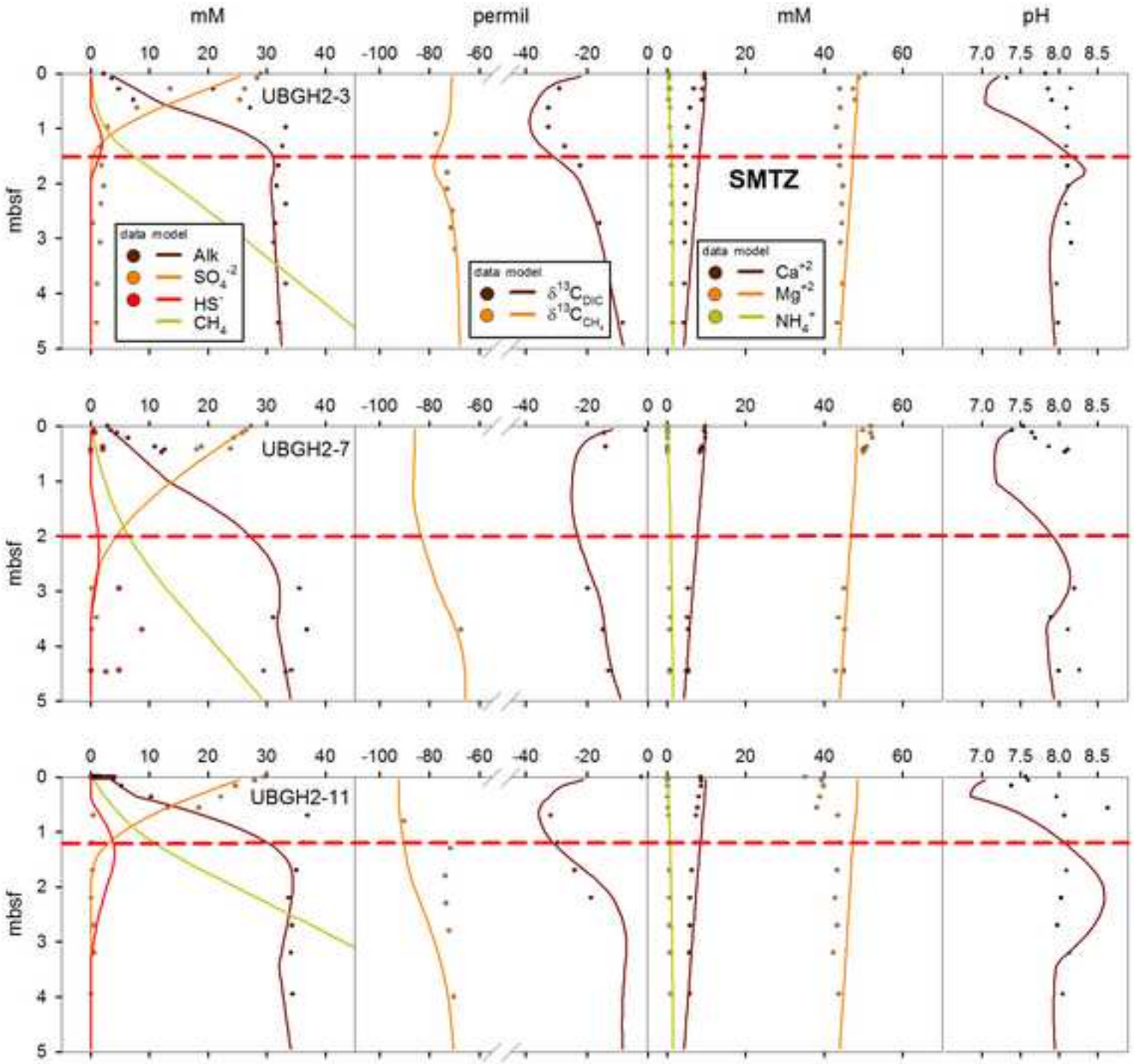

Fig4a

Click here to download high resolution image

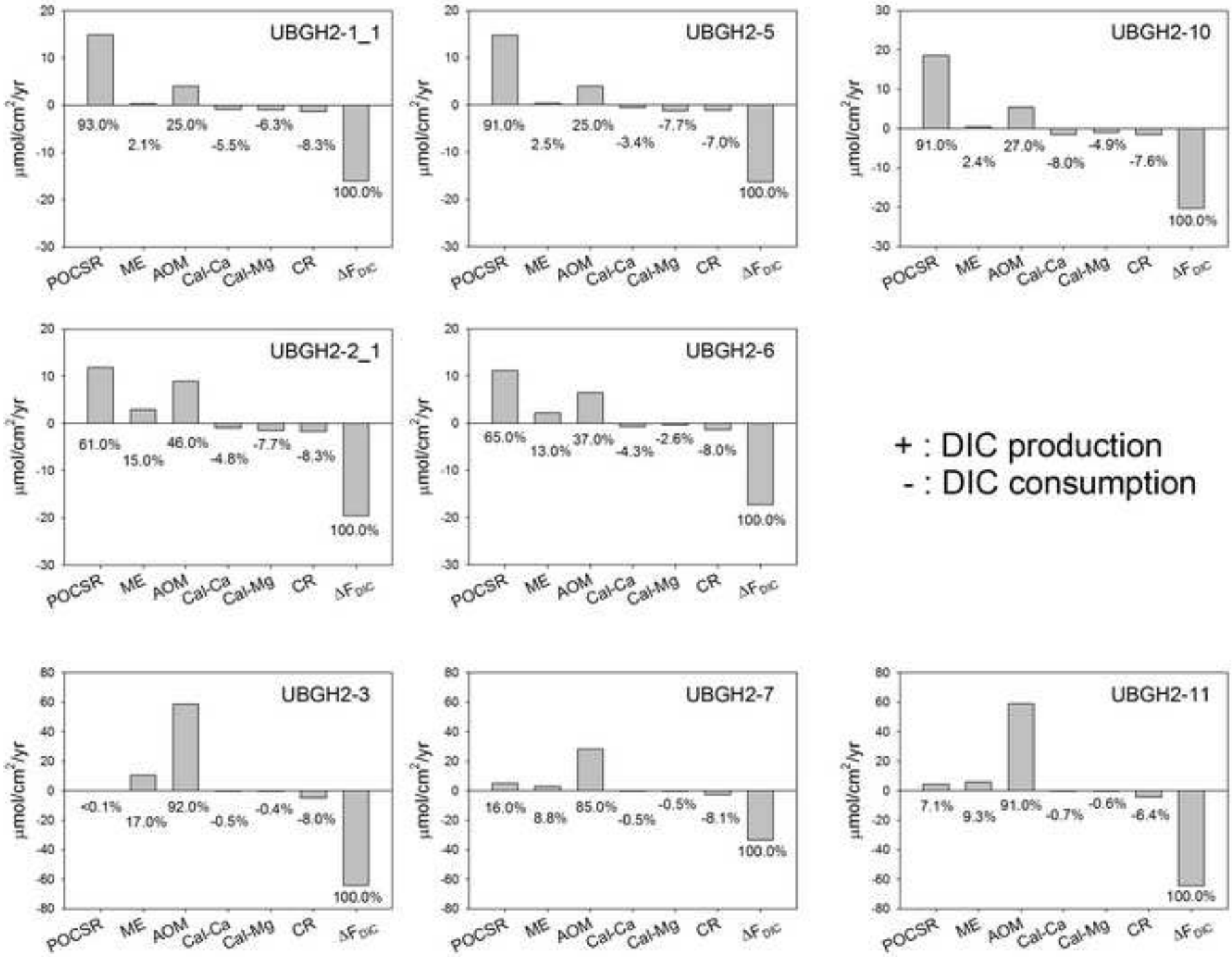

Fig4b

Click here to download high resolution image

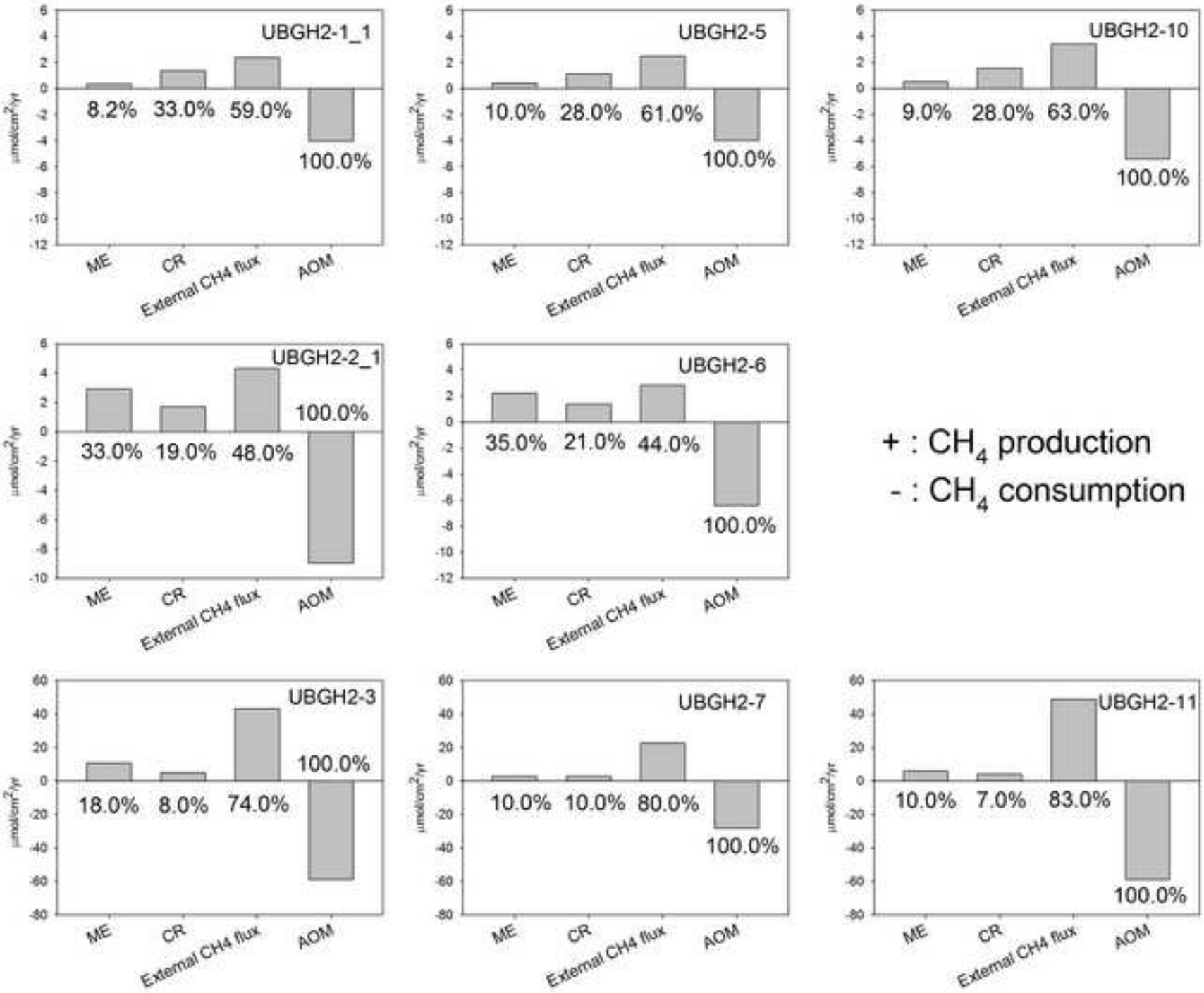

Fig4c

Click here to download high resolution image

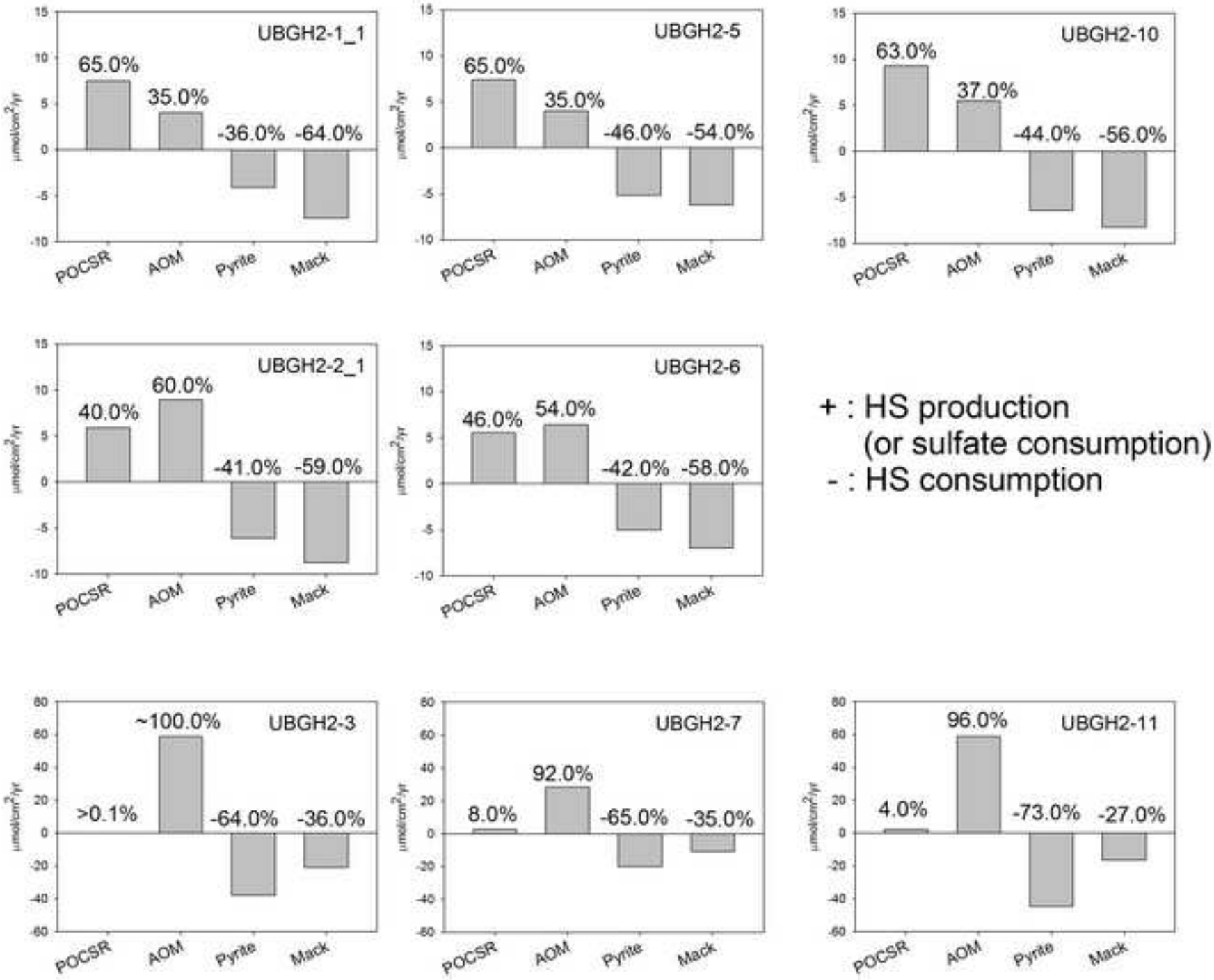

Fig5
Click here to download high resolution image

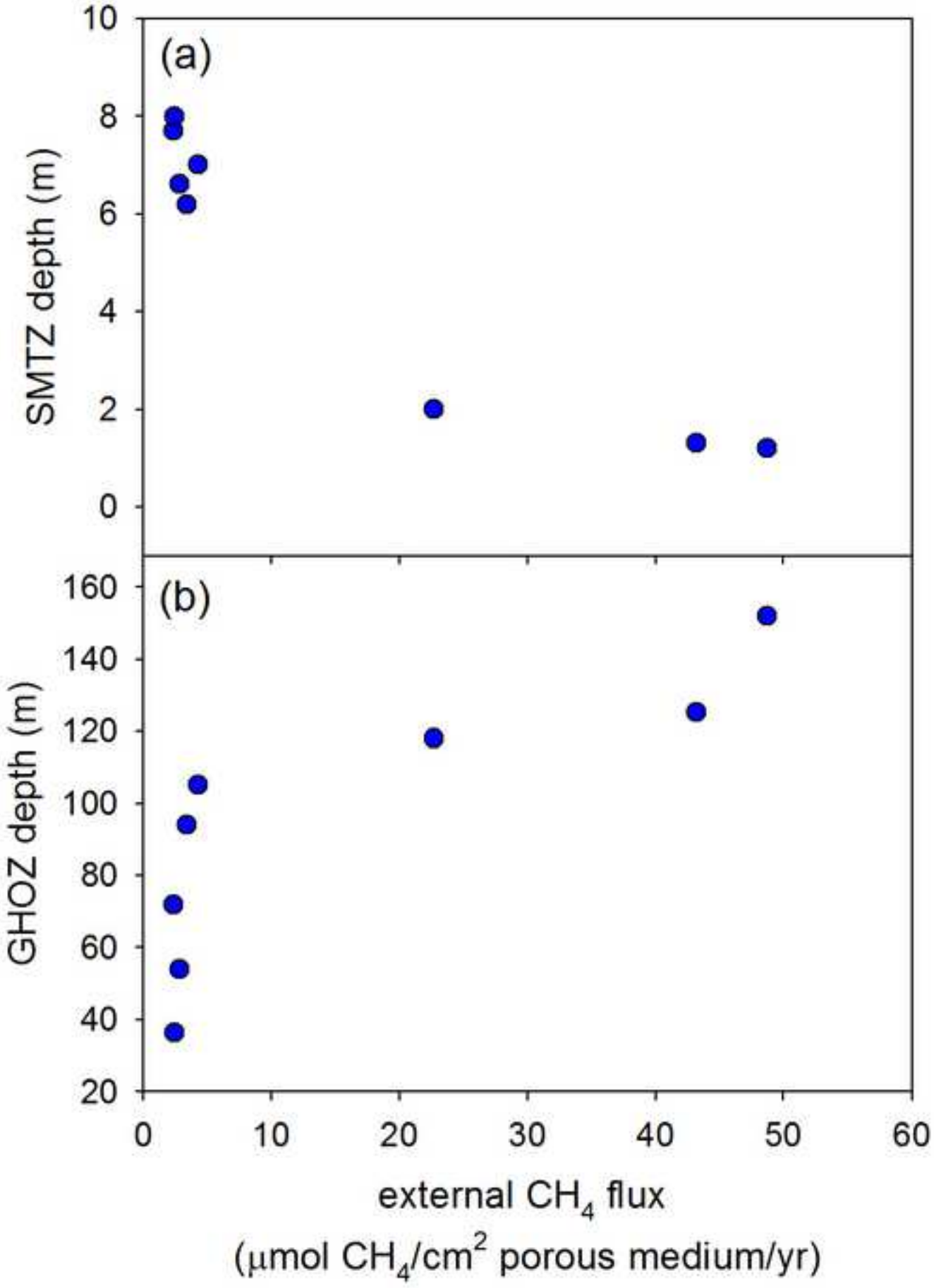

Fig6

Click here to download high resolution image

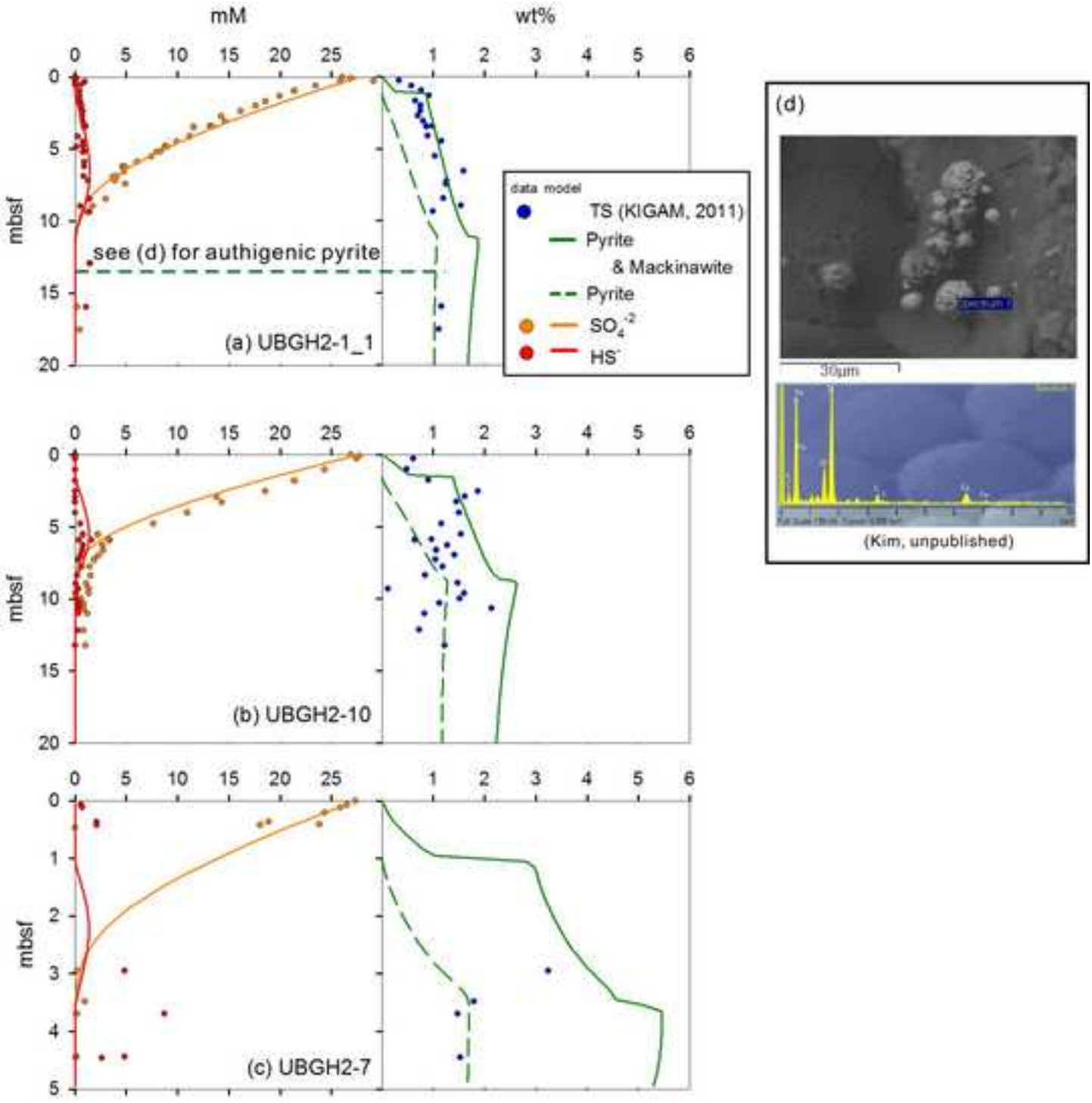

Fig7

Click here to download high resolution image

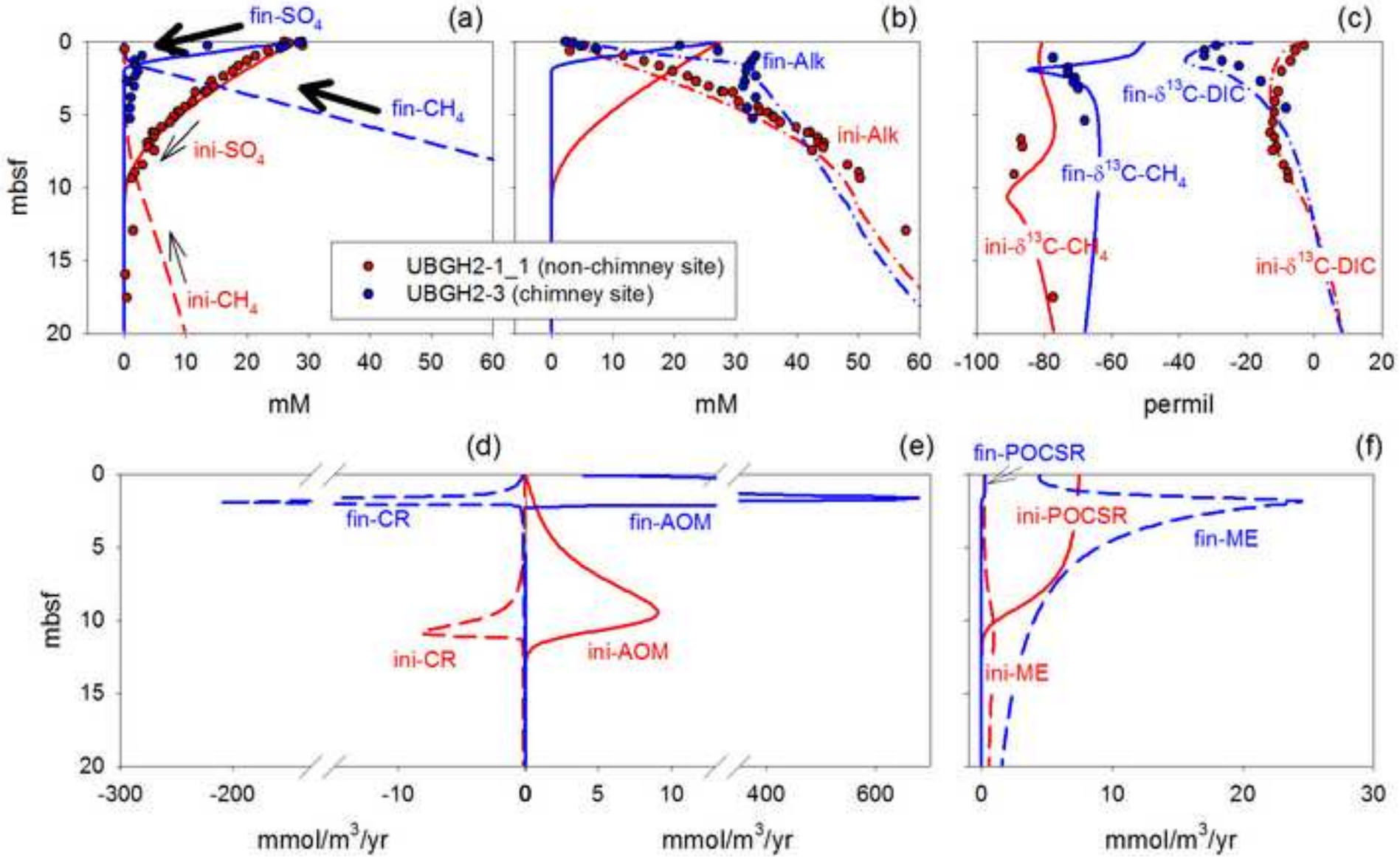

Fig8

Click here to download high resolution image

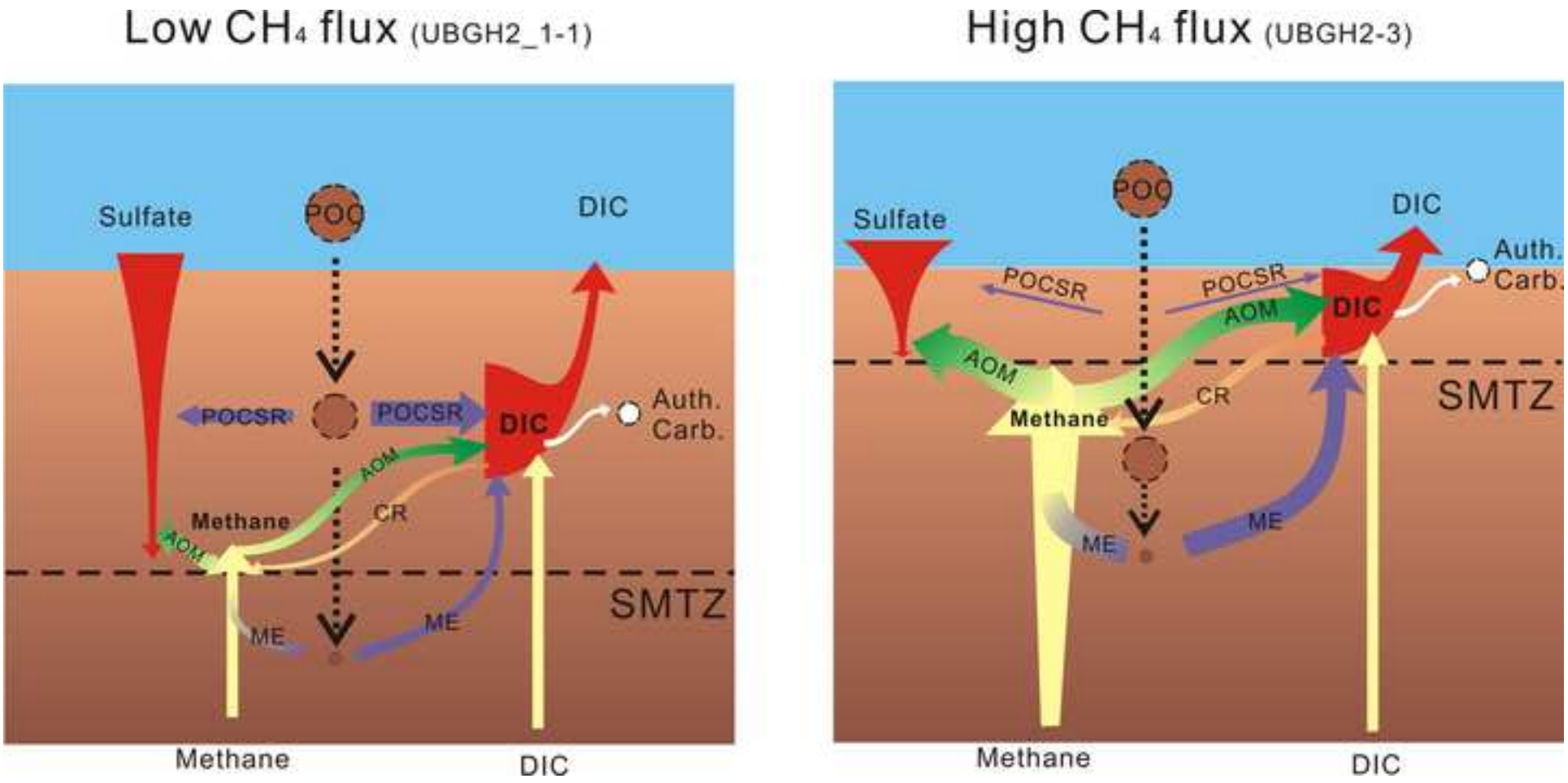

**Appendix1**

**Click here to download Appendix: Appendix1.doc**

**Appendix2**

**Click here to download Appendix: Appendix2_Hong_etal_UBGH2-1_1.pdf**

**Appendix3**

**Click here to download Appendix: Appendix3_Hong_etal_Crunchflow.pdf**